MEASURING $D_\perp$ AND $\chi_\perp$ IN THE HSX EDGE

by

Laurie A. Stephey

A masters project report submitted in partial fulfillment of
the requirements for the degree of

Masters of Electrical Engineering

(Electrical Engineering)

at the

UNIVERSITY OF WISCONSIN–MADISON

2013

DISCARD THIS PAGE

TABLE OF CONTENTS

ABSTRACT

Stellarator design has substantially improved over the past decade, but stellarator edge physics, especially in terms of heat and particle exhaust, is still not well-understood. Codes such as EMC3-EIRENE [8] are being used to model 3D edge physics, but these simulations must be informed by experimental measurements. Two important quantities that will be measured in the HSX edge are the perpendicular particle diffusivity, $D_\perp$, and the perpendicular thermal diffusivity, $\chi_\perp$. This work includes a comprehensive literature review, calculations that show that power deposition measurements are possible in HSX, preliminary diagnostic and experimental design ideas, and an outline for what will become a dissertation topic.

Experiment	Date	$D_\perp$ (m^2 s^{-1})	$\chi_\perp$ (m^2 s^{-1})
JET	1988	0.1-10	
JT-60U	1992		2-6
ASDEX	1992	0.5-2.5	
ASDEX-U	1995	0.1-0.3	0.25-1.5
JET	1998		0.05-1.0
C-MOD	2000	0.01-1	0.1-0.5
W7-AS	2001	0.4-0.8	1.2-2.4
DIII-D	2003	0.08-0.15	0.25-0.8
TEXTOR	2003	0.2	
JET	2004	1	
LHD	2006	0.1-0.8	

Table 0.1 Values of $D_\perp$ and $\chi_\perp$ from the literature. [2, 7, 11, 13–20]

0.1 Introduction

Recent advances in stellarators have prompted the need to better understand edge physics for purposes of heat and particle exhaust. Codes such as EMC3-EIRENE [8] are being used to model 3D edge physics and can provide important insights about edge flows, island structures, power deposition, and neutral particle interaction. However, experimental measurements must be used to guide such computational studies.

Two important pieces of the edge physics puzzle are the perpendicular particle diffusivity, $D_\perp$, and the perpendicular thermal diffusivity, $\chi_\perp$. Together, these values determine the nature of edge behavior. Experimental values of these perpendicular transport coefficients vary between experiments and also within experiments. Measured values from the literature are cataloged in Table 0.1.

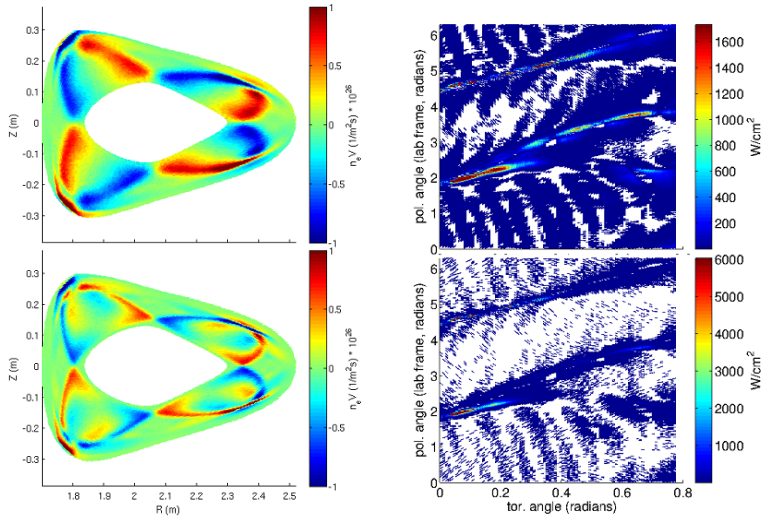

Figure 0.1 EMC3-EIRENE calculations for HSX courtesy of A. Bader. The left plots are $n_e V_\parallel$ for a large island configuration. The right plots are power deposition on the wall for a small island configuration. $D = 1.0$ m^2/s in the top plots and $D = 0.25$ m^2/s in the bottom plots. In these simuulations, $\chi_\perp = 3D_\perp$. [1]

In EMC3-EIRENE, $D_\perp$ and $\chi_\perp$ are both adjustable user inputs. Typically $\chi_\perp = 3D_\perp$, although each parameter can be varied independently. One of the goals of this research will be to determine if the common assumption $\chi_\perp = 3D_\perp$ is in fact a good approximation.

If $D_\perp$ and $\chi_\perp$ are small, the edge structures are very clear and well-formed. If these coefficients are large, the edge structures become blurred and there are no sharp boundaries between flow structures, islands, or regions of high power-deposition. This is illustrated for HSX in Fig. 0.1. Consequently, it is very important that the values of $\chi_\perp$ and $D_\perp$ used in these simulations are informed by experiment.

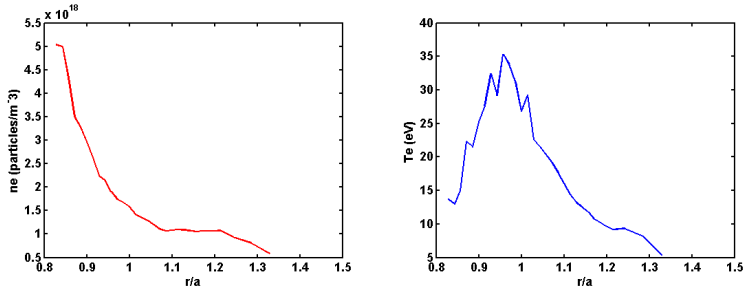

Figure 0.2 Triple-probe edge measurements courtesy of B. Wilcox. These measurements were made in the HSX outboard midplane in the QHS configuration. These measurements will be compared to EMC3-EIRENE predictions for various values of $D_\perp$ and $\chi_\perp$.

0.2 Initial probe comparisons

A relatively straightforward first step is to compare measurements which have already been made to EMC3-EIRENE predictions of edge temperature and density. B. Wilcox has measured the HSX edge temperature and density profiles at the outboard midplane with a triple probe. These measurements are shown in Fig. 0.2.

These measurements will be compared to EMC3-EIRENE predictions with various values of $D_\perp$ and $\chi_\perp$. This comparison will provide some insight into how the values of these coefficients are expected to impact the edge gradients. A second set of radial measurements of T_e and n_e at the top of the HSX boxport may soon be available for additional comparison courtesy of A. Akerson. These measured edge gradients will be able to provide some constraints on the values of $D_\perp$ and $\chi_\perp$.

Since stellarator edge behavior is complex, 1D radial measurements will not provide enough information to fully characterize $D_\perp$ and $\chi_\perp$. 2D measurements of the IR power deposition footprint can be used to determine $\chi_\perp$ and similarly, 2D measurements of the hydrogen/impurity line emission footprint can be used to determine $D_\perp$. In the following sections, both measurements will be described in detail.

Measurable range	3.6-5 μm
Refresh rate	60 Hz
Precision	0.1 °C
Accuracy	$\pm$ 2°C

Table 0.2 HSX FLIR Prism DS IR Camera specifications

0.3 Infrared power deposition measurements to determine $\chi_\perp$

Infrared measurements can be used to infer a value of $\chi_\perp$, the perpendicular thermal diffusivity. This measurement can be compared to the EMC3-EIRENE predictions. A parameter scan of the value of $\chi_\perp$ will be used to find the value that yields the closest agreement with the measured footprint. This value will be the value of $\chi_\perp$ in the HSX edge.

0.3.1 Preliminary calculations

Preliminary calculations were necessary to first determine if power deposition measurements are feasible in HSX. Since IR cameras measure ΔT, the temperature rise of a target with a known thermal emissivity, this temperature rise must fall within the resolvable range of an IR camera. Specifications for the HSX IR camera are summarized in Table 0.2. Predicted temperature rise calculations for both the HSX vacuum vessel and limiter are detailed below.

In a typical HSX plasma shot with 100 kW of launched RF power, approximately 96 kW are delivered by the RF system to HSX. Of this 96 kW, approximately 25 percent (a conservative assumption) is absorbed by the plasma and another 15 kW is radiated by the plasma. This leaves approximately 10 kW to be deposited by the plasma. HSX plasma shots are typically 50 ms long, so in a typical HSX shot, approximately 500 J of energy are deposited by the plasma. The predicted temperature rise due to this deposited energy is calculated for both the HSX vacuum vessel and a target.

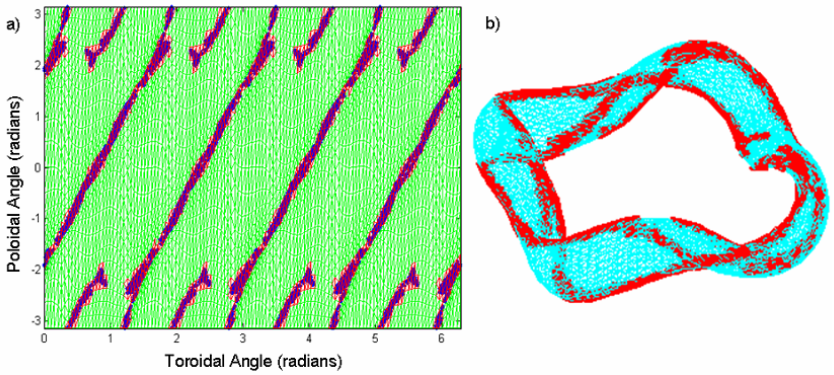

Figure 0.3 Calculation by J. Canik of the strike points in the HSX vacuum vessel. This calculation followed particles from 2 cm outside the HSX separatrix until they collided with the vacuum vessel. [3]

Emissivity	0.55
Heat capacity	0.5 J/g/°C
Thermal diffusivity	4.2 mm^2/s
Density	7600 kg/m^3

Table 0.3 Properties of stainless steel

0.3.2 Power deposition footprint on the HSX vacuum vessel

The HSX vacuum vessel is $1/4$ inch stainless steel. Relevant properties of stainless steel are listed in Table 0.3. The surface area of the HSX vessel is approximately 10.5 m^2.

The thermal diffusivity of an material, α, is approximately the rate at which heat can spread through it. Its relationship with temperature, distance, and time is summarized in the heat equation:

$$\frac{\partial T}{\partial t} = \alpha \nabla^2 T \tag{0.1}$$

When solved, this equation shows that L, the characteristic distance heat can travel, is approximately

$$L = \sqrt{\alpha t} \tag{0.2}$$

Surface Area	Area (m^2)	Mass (kg)	Blackbody Rise (°C)	Actual Rise (°C)
5 %	0.525	1.827	0.547	0.301
10 %	1.05	3.655	0.274	0.151
25 %	2.625	9.137	0.109	0.060
50 %	5.25	18.27	0.055	0.030

Table 0.4 Predicted temperature rise for several fractions of surface area of the HSX stainless steel vacuum vessel.

This means that for the HSX vacuum vessel, heat can travel approximately 0.458 mm during a 50 ms shot. As a result, the HSX vacuum vessel appears to be approximately 0.458 mm thick, roughly 7 percent of the total vessel thickness. It is believed that the power is deposited on the HSX vacuum vessel in a strike point pattern (shown in Fig. 0.3) generated by following particles along a field line outside the separatrix. If the value of $\chi_\perp$ was equal to zero, the heat deposition would fall exactly on these strike points. If the value of $\chi_\perp$ is larger, the deposition will be spread over a greater surface area. Table 0.4 summarizes calculations for heat deposition on 5, 10, 25, and 50 percent of the surface area of the HSX vacuum vessel.

These calculations indicate that measuring such small temperature rises on the HSX vacuum vessel would be difficult. The predicted temperature rise values are at the limit of the resolvable range of the current HSX IR camera; making these measurements would likely require a significantly more sensitive IR camera.

0.3.3 Power deposition footprint on the HSX limiter

We now consider the predicted temperature rise on the HSX limiter. This graphite limiter is approximately 40 cm^2 and is located at the top of HSX boxport C. Relevant properties of graphite are listed in Table 0.5. As above, we calculate that in a 50 ms shot, the thickness of the limiter appears to be approximately 0.424 mm.

C. Clark has calculated that when inserted 1 cm into the HSX plasma, the limiter intercepts 45 percent of field lines. Assuming that the heat is distributed evenly throughout the field lines, the

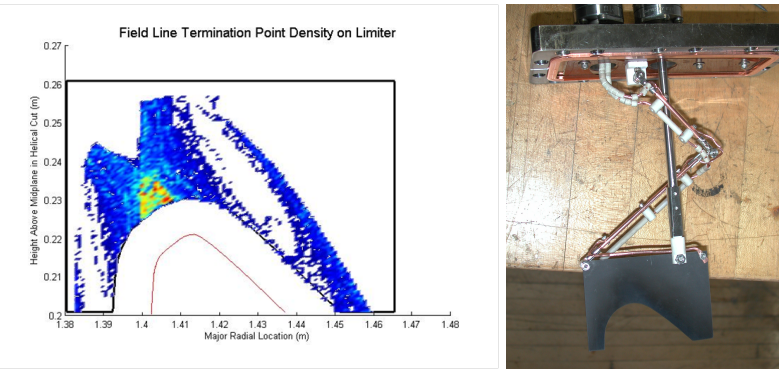

Figure 0.4 (left) Calculation by C. Clark of the field line termination point density on the HSX limiter. These calculations show that 45 percent of field lines are intercepted by the limiter when inserted 1 cm into the HSX plasma. Additionally, they indicate that a 2D footprint pattern may be observed. (right) A photograph of the actual HSX limiter. Signs of erosion/deposition are visible at the inner edge of the limiter, suggesting that the field line termination pattern is similar to what is predicted.

Emissivity	0.7
Heat capacity	0.71 J/g/°C
Thermal diffusivity	3.6 mm^2/s
Density	2.1 g/cm^3

Table 0.5 Properties of graphite

limiter would absorb 225 J during a plasma shot. Table 0.6 summarizes the predicted temperature rise of the limiter. These calculations indicate that the predicted temperature rise of the limiter, approximately 60°C, should be well within measurement limits. C. Clark also calculated the field line termination point density on the limiter shown in Fig. 0.4. This calculation suggests that a 2D footprint pattern should be measurable on the HSX limiter with the largest emission values closest to the plasma. Photographs of the limiter after it was installed in HSX indicate indicate that there is erosion/deposition occurring at the inner edge of the limiter as predicted.

Using the limiter rather than the HSX vessel wall as a target has the additional advantage that it can be very precisely spatially localized. It can also be moved radially in and out of the plasma

Area (cm^2)	Mass (g)	Blackbody Rise (°C)	Actual Rise (°C)
40	3.528	88.98	62.28

Table 0.6 Predicted temperature rise for the HSX limiter.

and the SOL to study the "focusing" behavior of the field lines and to study the edge parameters as a function of this focusing and of radial position.

TEXTOR [9] has successfully used an IR camera to measure the power deposition footprint on its Dynamic Ergodic Divertor (DED). An IR image that has been mapped into toroidal and poloidal coordinates is shown in Fig. 0.5. Temperature rises of 80 to 140 °C were measured and a helical pattern can be observed.

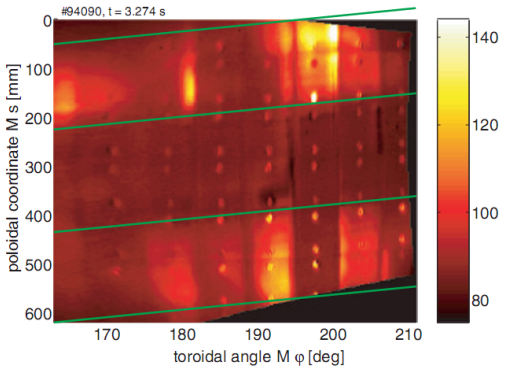

Figure 0.5 IR image of TEXTOR DED divertor. [9] The green lines guide the eye along the helical stripes.

To make a comparison between experimentally measured temperature rise and heat flux, a 2D heat conduction code such as THEODOR [12] or a 3D heat conduction code such as TACO [4], both of which are currently being used at NSTX and other experiments, can be used to calculate the heat flux profile on the limiter from the measured surface temperature. This calculated heat flux profile can then be directly compared to simulated heat flux profiles from EMC3-EIRENE.

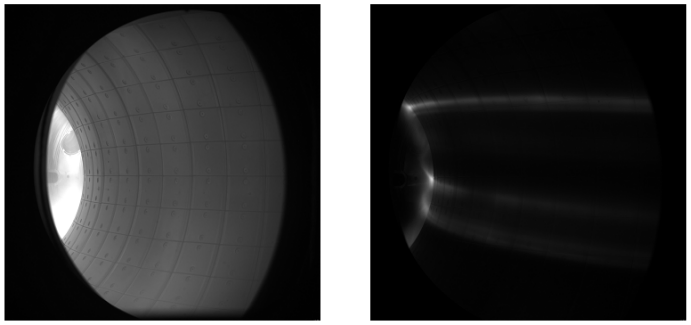

(a) Spectrally unfiltered image with homogeneous illumination of the target tiles during the breakdown of the discharge.

(b) C II (514 nm) emission during divertor operation (#106585).

Figure 0.6 An unfiltered image (a) and a C-II optically filtered image (b) of the TEXTOR divertor during operation. [5]

0.4 Line emission measurements to determine $D_\perp$

Neutral species line emission measurements can be used to infer the value of the perpendicular particle diffusivity, $D_\perp$. These 2D line emission measurements can be compared to the EMC3-EIRENE predictions. A parameter scan of the value of $D_\perp$ will be used to find the value that yields the closest agreement with the measured footprint. This value will be the value of $D_\perp$ in the HSX edge.

Both hydrogen (H-alpha) and carbon (C-II or C-III) emission will be measured since it is not yet known which line(s) can provide the best measurement fidelity. Since the HSX limiter is made of graphite, plasma particles will cause physical carbon sputtering when they collide with the limiter. Other experiments, including TEXTOR [5], have successfully used this technique. Measuring H-alpha emission may also provide localized particle deposition information.

0.4.1 Using EMC3-EIRENE output to generate synthetic emission images

H. Frerichs et al. have demonstrated a method to generate synthetic H-alpha emission from EMC3-EIRENE outputs. [10] A comparison between measured and synthetic emission is shown in Fig. 0.7. H. Frerichs has recently provided these modules to A. Bader, a collaborator on this research, who has been able to implement them for HSX simulations. These modules can be

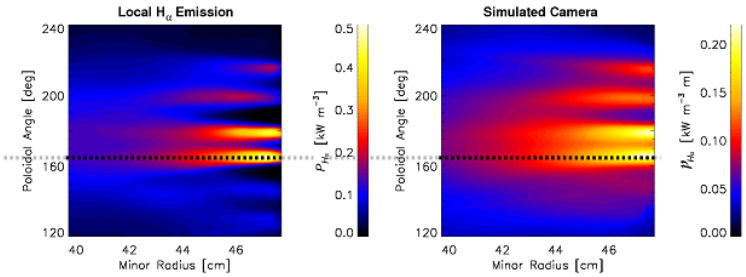

Figure 0.7 (left) A mapped image of measured H-alpha emission. (right) A simulated camera image generated by Frerichs et. al by using EMC3-EIRNE outputs. [10]

used as a synthetic diagnostic to predict line emission for all species of interest. This synthetic emission can then be directly compared to the camera measurements.

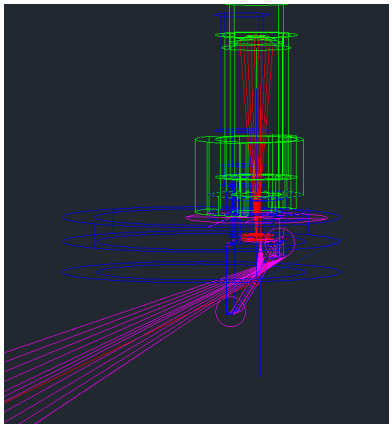

Figure 0.8 The HSX CHERS system toroidal view. It is installed in field period B and is designed to image the CHERS beam near boxport B. This design will be used as a guide to design the IR-CCD camera diagnostic.

0.5 Preliminary diagnostic design

To make measurements of the 2D footprint on the limiter, a view for the camera roughly perpendicular to the surface of the limiter will be required. The HSX limiter is located at the top of boxport C and there are currently no ports available that can directly provide this perpendicular view. However, the 8 inch port in field period C is available and by using a mirror in very much the same manner as the CHERS toroidal view (pictured in Fig. 0.8), we believe we can provide a nearly perpendicular view of the limiter. Using AutoCad, we will first verify that this view is possible from the 8 inch port. We will then use the CHERS system as a template to design a mirror system that is capable of imaging the limiter.

We will be begin by making measurements of the IR emission from the limiter. This will require a mirror system that is reflective in the IR and also a special window, such as sapphire, that is transparent in the IR. Once the internal mirror system is installed, an external mount will be designed so that the camera can view the limiter.

Once this concept has been successfully used to measure and characterize the IR footprint under a variety of experimental conditions, we can switch the system to make a particle emission measurement. If we design the system with this dual-purpose measurement in mind (i.e. using

wideband windows and mirrors), only the camera and optical filters will need to be changed. The appropriate optical filter for each emission line can be inserted to provide filtered light to a CCD camera and obtain a 2D image of the footprint on the limiter.

0.5.1 Mapping measured image into grid coordinates

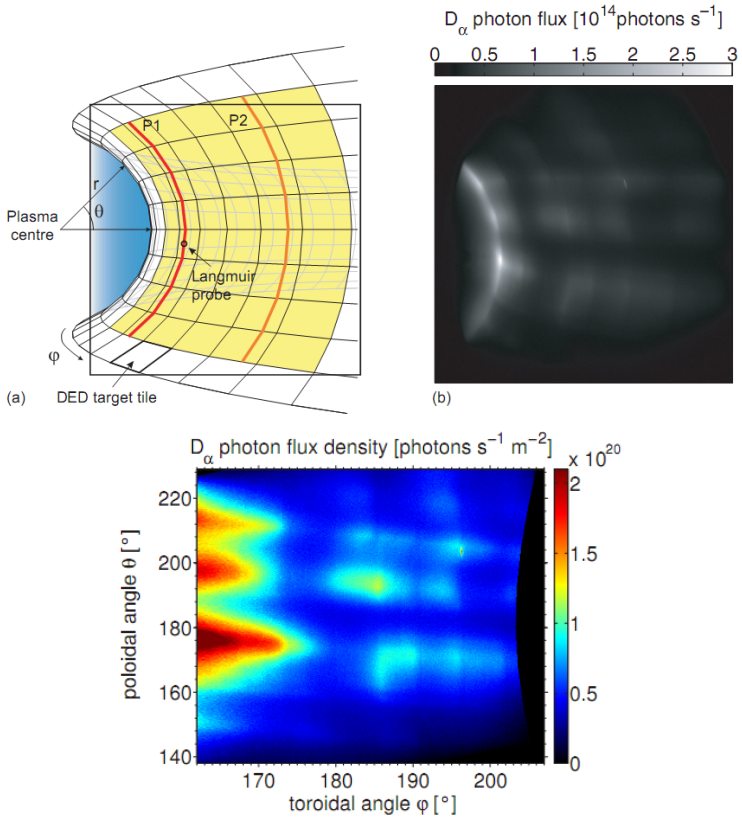

Figure 0.9 This figure illustrates the process used by Clever to map an image into poloidal and toroidal coordinates. [5, 6]. The LEOPOLD grid is shown in (a) on the top left. Once this grid was created, the measured photons were mapped into the grid (shown in (b) on the top right). The LEOPOLD code was then used to map the pixels into poloidal and toroidal coordinates (shown on the bottom).

Once this footprint measurement is made, it will be necessary to use image-processing to transform the emission into coordinates which can be easily be compared to EMC3-EIRENE calculations. A software package such as AutoCad Inventor and an image mapping code will

be necessary to map the image pixels from lab coordinates to poloidal and toroidal coordinates. Once this mapping has been accomplished, the measured and synthetic emission can be directly compared.

This procedure was successfully used by Clever in his dissertation work at TEXTOR. Fig. 0.9 is taken from Clever's thesis and subsequent publication and depicts how CCD camera images were transformed from lab space to poloidal and toroidal coordinates using the image mapping code LEOPOLD. [5, 6] LEOPOLD currently appears to be managed by T. Eich at the Max Plank Institute in Garching.

0.6 $D_\perp$ and $\chi_\perp$ parameter dependencies

One of the major goals of this work is to explore the dependencies of $D_\perp$ and $\chi_\perp$ on various HSX parameters:

- Magnetic configuration

  Small islands (QHS)

  Large islands (9% Hill)

  Connection length distribution

- Magnetic field strength (0.5 and 1.0 T) (observed at LHD [20])
- Heating power (50 and 100 kW)
- Radial position of limiter
- Central T_e and n_e (observed at LHD [20] and W7-AS [11])

0.7 Summary

The goal of this work will be not only to make measurements of $D_\perp$ and $\chi_\perp$ in the HSX edge, but also to determine the parameter dependencies and the basic physics (i.e. neoclassical or turbulent transport) that govern these quantities. Does the common assumption $\chi_\perp = 3D_\perp$ hold? Can $\chi_\perp$ be experimentally increased to increase the plasma wetted area, as will be required in a true reactor? This study will aim to address these as yet unanswered questions.

LIST OF REFERENCES

[1] A. Bader, D. T. Anderson, and C. C. Hegna et al. Simulations of edge configurations in quasi-helically symmetric geometry using EMC3-EIRENE. *Submitted to J. Nucl. Fusion*, 2013.

[2] H. S. Bosch, J. Neuhauser, and R. Schneider et al. 2D modeling of the ASDEX-Upgrade scrape-off layer and divertor plasma. *J. Nucl. Mat.*, pages 558–562, 1995.

[3] J. M. Canik. *Experimental verification of reduced particle and electron heat transport with Quasisymmetry in the HSX stellarator*. PhD thesis, Univeristy of Wisconsin - Madison, 2007.

[4] G. Castle. Theory and operating instructions for the taco run code. *UKAEA Fusion*, COMPASS Note 97.16, 1997.

[5] M. Clever. *Hydrogen recycling and transport in the helical divertor of TEXTOR*. PhD thesis, Heinrich-Heine-Univeritat Dusseldorf, 2010.

[6] M. Clever, S. Brezinsek, and H. Frerichs et al. Experimental investigation of density regimes in the helical divertor at TEXTOR. *J. Nucl. Fusion*, 52(054005), 2012.

[7] S. K. Erents and P. C. Stangeby. Heat transport in the JET scrape-off layer. *J. Nucl. Fusion*, pages 1637–1650, 1998.

[8] Y. Feng, F. Sardei, and J. Kisslinger et al. 3D edge modeling and island divertor physics. *Contrib. Plasma Physics*, 44:57–69, 2004.

[9] K. H. Finken, S. S. Abdullaev, and W. Biel et al. The dynamic ergodic divertor in the TEXTOR tokamak: plasma response to dynamic helical magnetic field perturbations. *Plasma Physics and Contr. Fusion*, 46:B143–B155, 2004.

[10] H. Frerichs, D. Reiter, and M. Clever et al. Three-dimensional computer simulations of local and line-of-sight integrated H_α line emission in the TEXTOR helical divertor. *37th EPS Conference on Plasma Physics*, (P2.127), 2010.

[11] F. Gadelmeier, Y. Feng, and P. Grigull et al. Conditions for island divertor operation in the W7-AS stellarator. *28th EPS Conference on Contr. Fusion and Plasma Phys.*, 25A:2085–2088, 2002.

[12] A. Herrmann, W. Junker, and K. Gunther et al. Energy flux to the ASDEX-upgrade diverter plates determined by thermography and calorimetry. *Plasma Phys. Control. Fusion*, 37:17–29, 1995.

[13] A. Kallenbach, Y. Andrew, and M. Beurskens et al. EDGE2d modelling of edge profiles obtained in JET diagnostic optimized configuration. *Plasma Phys. and Contr. Fusion*, 46:431–446, 2004.

[14] B. LaBombard, M. V. Umansky, and R. L. Boivin et al. Cross-field plasma transport and main-chamber recycling in diverted plasmas on Alcator C-Mod. *J. Nucl. Fusion*, 40:2041–2060, 2000.

[15] M. Lehnen, M. Brix, and U. Samm et al. Plasma edge transport phenomena caused by particle drifts and sources in TEXTOR. *J. Nucl. Fusion*, pages 168–178, 2003.

[16] K. McCormick, G. Kyriakakis, and J. Neuhauser et al. Particle and energy transport scalings in the ASDEX scrape-off layer. *J. Nucl. Mat.*, pages 264–270, 1992.

[17] A. Y. Pigarov, S. I. Krasheninnikov, and W. P. West, et al. DIII-D edge plasma simulations with UEDGE code including non-diffusive anomalous cross-field transport. *J. Nucl. Mat.*, pages 1076–1080, 2003.

[18] K. Shimizu, K. Itami, and K. Hirotaka et al. Transport analysis of divertor plasma in JT-60U. *J. Nucl. Mat.*, pages 476–480, 1992.

[19] P. C. Stangeby, J. A. Tagle, and S. K. Erents et al. Measurements of the cross-field diffusion coefficient $D_\perp$ in the edge plasma of JET. *Plasma Phys. and Contr. Fusion*, 30:1787–1803, 1988.

[20] K. Tanaka, C. Michael, and A. L. Sanin et al. Experimental study of particle transport and density fluctuations in LHD. *J. Nucl. Fusion*, 46:110–122, 2006.